COVER SHEET

Confirmation Number: **21**

Title: **An Engineering Approach to Analyze Damage Initiation Modes in Tapered Composite Structures**

Authors: Prabhakar M. Rao[1]
Upul R. Palliyaguru[2]
Mark R. Gurvich[1]
Waruna Seneviratne[2]

ABSTRACT

In this work an engineering approach is demonstrated for analyzing damage initiation modes in tapered composite structures. The analysis methodology includes simulation of the non-linear static response of tapered composite structures under static tension loads to predict the location of interfacial delamination initiation. Furthermore, the developed methodology provides a strength-based criterion to assess whether damage initiation will occur in the inter-laminar delamination or intra-laminar matrix cracking mode. Based on the results of the analysis, a tapered composite structure is fabricated and tested under displacement-controlled quasi-static tension loading. The damage initiation location captured experimentally is compared with the analysis towards achieving preliminary qualitative validation. The linear stiffness of the tapered composite structure is predicted within 15% of the experimental average thereby achieving preliminary quantitative validation.

INTRODUCTION

Composite aerospace structures are composed of multiple ply-drops and pure resin pockets often incorporated to spatially vary the thickness of fabricated parts. These necessary manufacturing artifacts introduce largescale discontinuities leading to sharp gradients in the stress fields and associated stress concentrations. Consequently, damage is often initiated at the above discontinuities and may result in either progressive or sudden catastrophic failure. The capability to accurately predict the structural response and damage characteristics of these structures necessitates the development of advanced Progressive Damage Analysis (PDA) techniques that can capture damage initiation and growth.

1. United Technologies Research Center, 411 Silver Lane, East Hartford, CT 06108.
2. National Institute for Aviation Research, Wichita State University, 1845 Fairmount, Wichita, KS 67260.

The PDA techniques could be based on Continuum Damage Mechanics (CDM) [1, 2], Discrete Damage Mechanics [3–5] or a combination of the above [6]. Regardless of the mechanistic framework, independent Verification and Validation (V&V) [7, 8] of the PDA techniques needs to be performed for acceptance as a design tool. The V&V approach adopted herein is illustrated in Figure 1. A large body of work, for example [9–13], exists in the literature that details the V&V of PDA techniques at the 'Coupon' level of the building approach, Figure 1. More recently, as part of the NASA Advanced Composites Consortium (ACC) program, validation of PDA codes at the 'Sub-elements' level, Figure 1, based on CDM [14] and DDM [15, 16] techniques have been reported.

The current work, however, is focused on the analysis and design of a tapered laminated composite structure for achieving the broader goal of V&V of PDA codes at the 'Elements' level, Figure 1. For this purpose, it is envisioned to analyze, design, fabricate and test a three-dimensional (3D) tapered laminated composite structure incorporating a racetrack cross-section, Figure 1. The chosen structural geometry, Figure 1, incorporates essential features of a composite spar which is the main load bearing member in composite rotor blades. Rotor blade composite spars experience tensile, cyclic bending and torsional loads in service. In this work, a tapered flat-plate pathfinder element, Figure 2, incorporating the essential geometric characteristics of the larger 3D element is designed and fabricated. Success in capturing expected damage modes i.e. inter-laminar delamination initiation and intra-laminar matrix cracking in the pathfinder element would enable the design and fabrication of the 3D racetrack cross-section element.

Therefore, the objective of this work is centered on demonstrating an engineering approach to analyze damage initiation modes in the pathfinder element, Figure 2. The pathfinder element is composed of IM7/8552 unidirectional tape material and incorporates multiple blocks of dropped plies sandwiched between continuous plies, as shown in Figure 2.
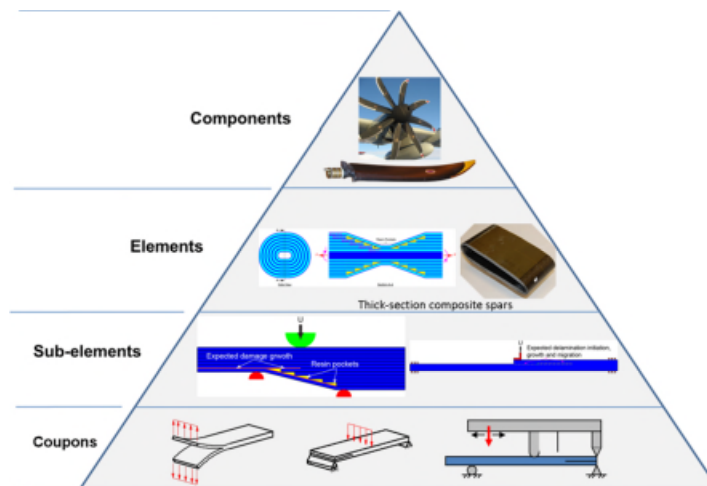

Figure 1. The building block approach for validating Progressive Damage Analysis (PDA) codes.

The techniques developed herein enable selection of the ±α angles and assessment of damage initiation and growth from the vicinity of the ply-drops. In such structures,

dominant damage modes include inter-laminar delaminations and intra-laminar matrix cracking [17]. However, from the standpoint of predicting the response of such structures, it is well-known that the ability to computationally capture intra-laminar damage modes is mesh-sensitive since the associated stress fields may be singular. Therefore, the methodology developed herein relies on separation of damage initiation into inter-laminar and intra-laminar modes. Relative to the applied loads, the damage mode that is triggered at the lowest load level is considered to be the dominant mode of damage initiation. The predictions obtained according to the developed approach are illustrated and correlated with experimental evidence for a representative tapered carbon/epoxy composite structure.
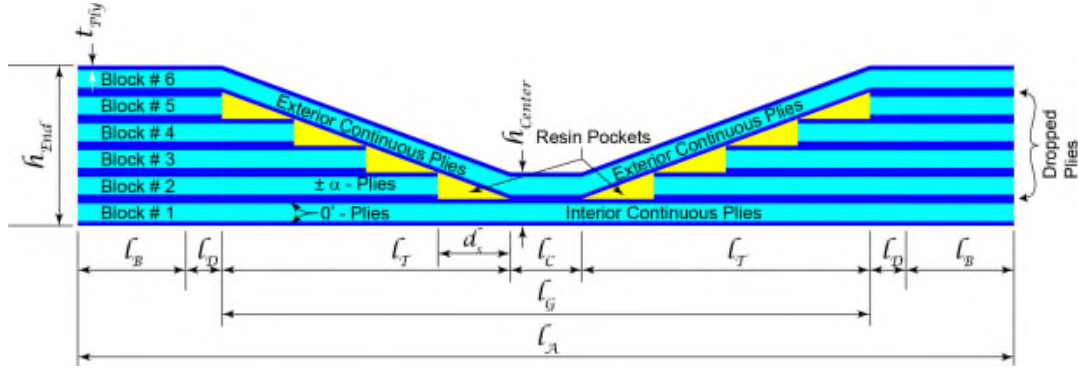

Figure 2. The composite pathfinder element with ply-drops showing resin pockets and continuous plies

PATHFINDER ELEMENT DESIGN

Geometric Dimensions

The focus of this section is to determine the geometric dimensions listed in Figure 2. The thickness of individual plies, t_{ply} is taken as 0.0073 in. (0.185 mm). In Figure 2, ℓ_B and ℓ_D correspond to the dimensions of the grip and load transfer transition regions, respectively. The transition regions are included to avoid failure in the vicinity of the grips. Based on previous experience, ℓ_B is taken to be 6.0 in. (152.40 mm) and ℓ_D is taken as 2.0 in. (50.80 mm) in this study.

In order to retain some definition of the resin pockets, the stagger distance d_s, was taken to be 1.625 in. (41.28 mm) in the study. As shown in Figure 2, the pathfinder element was designed using ply blocks, with the total number of such blocks taken as $n_B = 6$. Block # 1 and Block # 6 constitute the inner and exterior continuous plies, whereas Block # 2 through Block # 5 constitute the dropped plies, resulting in number of dropped ply blocks, $n_{DP} = 4$. The length of the tapered segment of the pathfinder element is then given by, $\ell_T = n_{DP} d_s$, whereas the length ℓ_C, representing the central transition region was taken to be 1.0 in. (25.40 mm) in this study. The dimension ℓ_G, is computed as $\ell_G = 2.0\ell_T + \ell_C = 14.0 \ in. (355.60 \ mm)$ and $\ell_A = \ell_G + 2(\ell_B + \ell_D) = 30 \ in. (762 \ mm)$.

The number of plies n_{ply}, in each block were chosen such that the thicknesses of the pathfinder element were reminiscent of composite rotor blade spars. As a result, the end thickness, $h_{End} = n_{ply} n_B t_{ply} = 6 \times 6 \times 0.0073 = 0.2628 \ in. (6.675 \ mm)$,

whereas, the central thickness, $h_{Center} = n_{ply}n_B t_{ply} = 6 \times 2 \times 0.0073 = 0.0876\ in.$ (2.225 mm).

Displacement-Controlled Static Tension Analysis

The structural response and damage characteristics of the pathfinder element were evaluated with two-dimensional (2D) plane strain half-symmetric models, Figure 3. For the purpose of predicting the location of inter-laminar delamination initiation, the above approximation of symmetry is assumed to be valid. The plies are modeled as linear elastic orthotropic continua with properties sourced from [18] wherein the $\pm\alpha$ plies are homogenized using Classical Lamination Theory (CLT). Intra-laminar failure is not modeled.
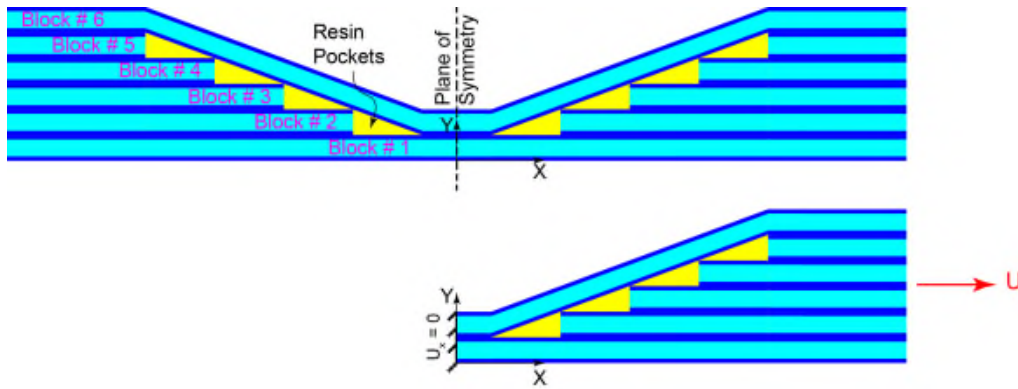

Figure 3. Half-symmetric 2D plane strain model of the pathfinder element. *Top:* Sketch of the pathfinder element showing assumed plane of symmetry. *Bottom:* The symmetric half model for displacement-controlled static tension analysis (Note: scales in X and Y directions are different).

Inter-laminar damage in the pathfinder element was modeled using the Cohesive Zone Method (CZM) wherein the initiation and growth was captured via a mixed-mode bi-linear traction-separation law [5]. Mode-I and Mode-II fracture toughness magnitudes i.e. $\mathcal{G}_{Ic}$ and $\mathcal{G}_{IIc}$ were sourced from [19] and [20], respectively. The Benzeggagh-Kenane (BK) [21] law for computing mixed-mode fracture toughness $\mathcal{G}_c$ assumed to be applicable for the interface regions. The corresponding Mode-I and Mode-II interface strengths i.e. Inter-Laminar Tensile (ILT) and Inter-Laminar Shear (ILS) strengths were sourced from [18]. Any potential effects of fiber-bridging were not considered.

The ABAQUS/Standard [22] commercial Finite Element (FE) program was used to execute the simulations. The cohesive contact capability built into ABAQUS [22] was used to model inter-laminar delamination initiation and growth in the pathfinder element. Details of the 2D plane strain models developed as part of this study showing the locations of the cohesive surfaces are illustrated in Figure 4.

Cohesive surfaces were included only along likely delamination regions, namely, Interface 1, Interface 2 and Interface 3, Figure 4. Along the global X-direction, each pure resin pocket was discretized with 500 2D plane strain reduced integration (CPE4R) elements, resulting in an element length of $\ell_x = 0.00325\ in.\,(0.083\ mm)$.

Previous studies [23] have shown that an element length of 0.00983 in. (0.25 mm) within the cohesive zone is sufficient to capture the far-field failure stress under pure Mode-II conditions as determined by Linear Elastic Fracture Mechanics (LEFM). In the through-thickness i.e. Y-direction as well, the mesh was made sufficiently fine as shown in Figure 4, to enable capturing the associated stress gradients.

The problem of predicting whether the inter-laminar or the intra-laminar damage mode would be triggered at a given load (displacement), was approached by developing a rudimentary strength-based criterion. This criterion evaluated a load factor, λ, defined as:

$$\ell_x = 0.00325 \; in.; \ell_y^{\pm\alpha} = 0.00292 \; in.; \ell_y^0 = 0.00146 \; in.$$
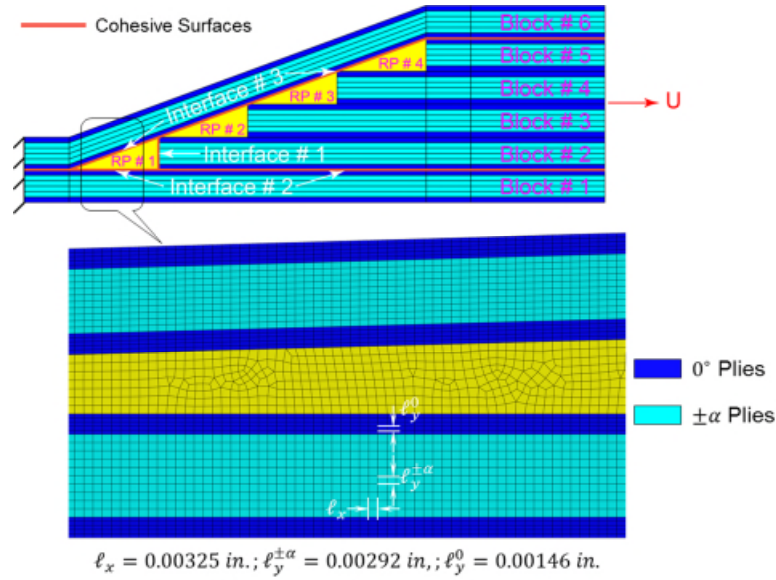
Figure 4. The 2D plane strain models developed to analyze the pathfinder element design for inter-laminar delamination initiation and growth. Individual Resin Pockets are labeled as RP #.

$$\lambda = \frac{X_T^{\pm\alpha}|_{CLT}}{S_{11}^{\pm\alpha}|_{Max}} \tag{1}$$

In Equation (1), $X_T^{\pm\alpha}|_{CLT}$ is the longitudinal strength of the off-axis $\pm\alpha$ ply stack computed with the aid of CLT. On the other hand, in Equation (1), $S_{11}^{\pm\alpha}|_{Max}$ is the maximum longitudinal tensile stress in the off-axis $\pm\alpha$ ply stack. $S_{11}^{\pm\alpha}|_{Max}$ is calculated at the lowest applied load (displacement) when the inter-laminar Cohesive Surface Damage ($CSDMG$) [22] variable attains a magnitude of 1.0 for any of the three interfaces shown in Figure 4. A Python program was written to parse the Output Database (ODB) files generated by ABAQUS [22] to determine the applied load (displacement) at which $CSDMG$ attained a value of 1.0, and the corresponding magnitude of $S_{11}^{\pm\alpha}|_{Max}$ for computing λ in Equation (1).

Computing the Longitudinal Tensile Strength of Off-axis Plies with CLT

The longitudinal tensile strength of the off-axis $\pm\alpha$ ply stack, $X_T^{\pm\alpha}|_{CLT}$, is calculated using the principles of CLT [24] in combination with the Factor of Safety (FS) [25, 26] defined as:

$$FS = \frac{\sigma_{Allowable}}{\sigma_{Design}} \tag{2}$$

In terms of the force resultants on a laminate, the longitudinal uniaxial tension loading case is given by: $N = \{N_x\ 0\ 0\}^T = \{1\ 0\ 0\}^T$. Then, the design stress in Equation (2) is the laminate average stress [24] given by:

$$\sigma_{Design} = \frac{N_x}{t_{\pm\alpha}} = \frac{1}{t_{\pm\alpha}} \tag{3}$$

In Equation (3), $t_{\pm\alpha}$ is the thickness of the $\pm\alpha$ plies stack. Using the Tsai-Hill failure criterion [24] to compute FS in Equation (2), it can be shown [26] that the longitudinal strength of the off-axis $\pm\alpha$ ply stack is given by:

$$X_T^{\pm\alpha}|_{CLT} = \sigma_{Allowable} = \frac{1}{\sqrt{\left[\frac{\sigma_{11}}{X}\right]^2 - \left[\frac{\sigma_{11}\sigma_{22}}{X^2}\right] + \left[\frac{\sigma_{22}}{Y}\right]^2 + \left[\frac{\tau_{12}}{S}\right]^2}}\left(\frac{N_x}{t_{\pm\alpha}}\right) \tag{4}$$

In Equation (4), X and Y are the in-plane longitudinal and transverse strengths, respectively, which assume tension and compression magnitudes in conjunction with the nature of the corresponding stress [26], whereas, S is the in-plane shear strength in Equation (4).

In order to verify Equation (4), $X_T^{\pm\alpha}|_{CLT}$ was calculated for a $\pm45°$ ply stack. For this case, $X_T^{\pm45}|_{CLT} = 27,000\ psi\ (186\ MPa)$, compares reasonably well with the corresponding experimentally determined strength $X_T^{\pm45}|_{Test} = 26,450\ psi\ (182\ MPa)$ [27]. The ratio of the above two strength magnitudes is defined as:

$$\Omega = \left(\frac{X_T^{\pm45}|_{Test}}{X_T^{\pm45}|_{CLT}}\right) = 0.98 \tag{5}$$

Parametric Studies for Selecting the Layup Sequence

Using the 2D plane strain FE models shown in Figure 4, parametric studies were performed with several different layup sequences to compute the parameter λ defined in Equation (1). The two key parameters chosen as part of these studies were, namely, the ply-drop stagger distance, d_s and the off-axis ply angle α. In each of these

simulations, $S_{11}^{\pm\alpha}|_{Max}$, in Equation (1) was computed for the homogenized off-axis ply stack using a Python program to parse the corresponding ODB file generated by ABAQUS/Standard. The knocked down longitudinal tensile strength for the same off-axis ply stack was then computed as:

$$X_T^{\pm\alpha}|_{KD} = \Omega X_T^{\pm\alpha}|_{CLT} \tag{6}$$

Subsequently, the parameter λ defined in Equation (1) was computed as:

$$\lambda = \frac{X_T^{\pm\alpha}|_{KD}}{S_{11}^{\pm\alpha}|_{Max}} \tag{7}$$

The outcomes of these parametric studies for $d_s = 1.625\ in.$ (41.275 mm) are provided in Table I. With reference to the discussions pertaining to Equation (1), any layup sequence for which $\lambda > 1.0$ would indicate a feasible layup, whereas, the case $\lambda < 1.0$ would imply an infeasible layup sequence. Herein, the feasibility of the layup sequence is taken as an indicator of the likelihood of the inter-laminar damage initiation mode being triggered at a given load (displacement). From the standpoint of maximizing the likelihood of inter-laminar damage initiation, the layup sequence with the maximum value of λ was chosen as part of this study. Therefore, the layup sequence in each ply block of the pathfinder element shown in Figure 3 is composed of on-axis 0° plies and off-axis $\pm 60°$ plies. The complete layup sequence for the pathfinder element is listed in Table II with the stagger distance between ply-drops, $d_s = 1.625\ in.\ (41.275\ mm)$.

TABLE I: DOWN-SELECTION OF THE LAYUP SEQUENCE AND STAGGER DISTANCE.

Ply Block Layup (deg.)	d_s (in.)	$S_{11}^{\pm\alpha}|_{Max}$ (psi)	$X_T^{\pm\alpha}|_{KD}$ (psi)	λ
[0/+30/+30/-30/-30/0]$_{6S}$	1.625	36458.27	35160.23	0.964
[-45/-45/+45/+45/0/0]$_{6S}$	1.625	25850.00	26450.00	1.023
[0/+60/+60/-60/-60/0]$_{6S}$	**1.625**	**9480.80**	**16604.83**	**1.751**
[0/+45/-60/-60+45/0]$_{6S}$	1.625	15351.64	21282.62	1.386

TABLE II: BLOCKWISE LAYUP OF THE PATHFINDER ELEMENT.

Block #1	Block #2	Block #3	Block #4	Block #5	Block #6
[0/+60/+60/-60/-60/0]	[0/-60/-60/+60/+60/0]	[0/+60/+60/-60/-60/0]	[0/-60/-60/+60/+60/0]	[0/+60/+60/-60/-60/0]	[0/-60/-60/+60/+60/0]

FABRICATION AND TESTING OF THE PATHFINDER ELEMENT

The pathfinder test article was fabricated using a vacuum bagging process and cured in the autoclave, per the cure cycle developed at the National Institute for Aviation Research (NIAR), Wichita State University (WSU) [28]. The outcome of the fabrication process highlighting the geometry of plies and resin is documented at the bottom of Figure 5. Individual photographs were manually grouped to create the composite image at the bottom of Figure 5. While it is necessary to evaluate the fabrication quality of the pathfinder along the width direction (perpendicular to the

plane of page), it is the geometry in the vicinity of the ply-drops that will drive the mechanics of the pathfinder under both static and fatigue tension loads.
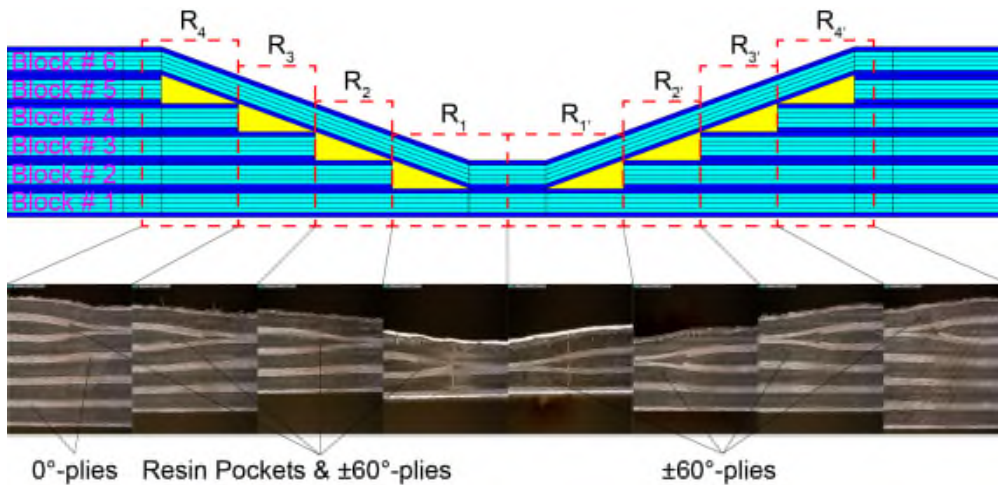

Figure 5. Comparison of the design and as-fabricated pathfinder test article.

The photograph at the bottom of Figure 5 reveals that the geometry of the on-axis 0°-plies and the off-axis ±60°-plies is mostly consistent with the design intent away from the vicinities of the ply-drops. However, the geometries of the resin pockets and ply-drops enclosed within the regions R_1 through $R_{4'}$ are quite different from the design intent. It is evident that both the 0°-plies and ±60°-plies have entered the designed pure resin pockets, and that it is nearly impossible to distinguish between the resin pockets and ±60°-plies in the vicinity of ply-drops. Therefore, it may be challenging to capture the location of damage initiation consistent with the design intent of the pathfinder element. Nevertheless, Non-Destructive Inspection (NDI) of the pathfinder article did not reveal any major largescale defects, pointing to the high quality of fabrication.
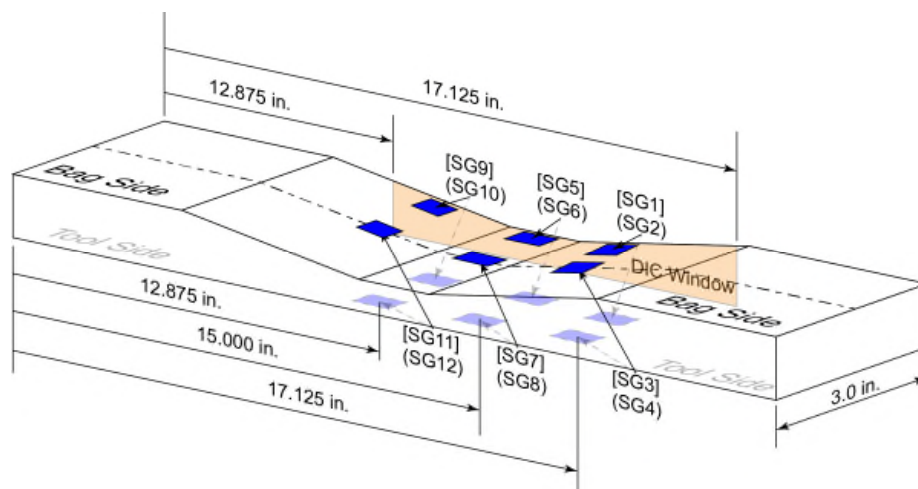

Figure 6. Location of strain gages on the pathfinder test article.

The pathfinder article was instrumented with strain gages measuring $0.25'' \times 0.18''$ ($6.35mm \times 4.57mm$), Acoustic Emission (AE) sensors and a Digital Image Correlation (DIC) data acquisition system. The locations of the strain gages (labeled [SG#] and (SG#)) and the DIC window are schematically illustrated in Figure 6. The AE sensors were installed on the tool side of the pathfinder article along the axial (i.e. length) direction, 1.0 in. (25.4 mm) from the near side shown in Figure 6. The locations of [SG1], [SG3], [SG9] and [SG11] correspond to the bag side interface of $R_1 - R_2$ and $R_{1'} - R_{2'}$ regions, whereas, the locations of (SG2), (SG4), (SG10) and (SG12) correspond to the tool side interface $R_1 - R_2$ and $R_{1'} - R_{2'}$ regions, Figure 5.

On the other hand, the locations of [SG5] and [SG7] correspond to the bag side interface of the $R_1 - R_{1'}$ regions, whereas, the locations of (SG6) and (SG8) corresponding to the tool side interface of the regions $R_1 - R_{1'}$, Figure 5. It was hypothesized that due to the tapered geometry of the pathfinder element, a net resultant moment will be induced leading to potential bending. Therefore, the strain gage installation in Figure 6 was chosen to enable capturing the aforementioned bending of the pathfinder.

The installation of the pathfinder in the testing machine and a representative photograph of the outcome of the static test are shown in Figure 7. A speckle pattern is spray painted onto the pathfinder article for capturing the deformation and strain fields via the DIC data acquisition technique. The photograph in Figure 7 (b) indicates that delamination failure mode is dominant near the top and bottom of the pathfinder, whereas, in the central thinner region, both matrix cracking and delamination failure modes are active, with matrix cracking being dominant. There is some evidence near the bottom of the photograph in Figure 7 (b) which suggests that the delamination failure mode is active in the vicinity of the ply-drop corresponding to the interface between regions $R_{1'}$ and $R_{2'}$ (see Figure 6), but the same cannot be conclusively proven based on Figure 7 (b). However, the overall delamination patterns and locations captured in the test seem to be consistent with the design intent of the pathfinder element.

The load-displacement data obtained from the test, Figure 8 (a), shows that response of the pathfinder is linear until the attainment of peak load, $P_{Exp}^{Max} = 25,000\ lbf$ (111,206 N), and thereafter the load drops suddenly. The sudden and total loss of load bearing capacity is indicative of unstable damage growth, thereby making it difficult to capture any progressive growth of damage modes. The measured load, P versus longitudinal strain ε_{11} data are shown in Figure 8 (b) for [SG3] and (SG4), in Figure 8 (c) for [SG7] and (SG8) and in Figure 8 (d) for [SG11] and (SG12), respectively. It is evident from the above figures that the corresponding gages record location-specific differential straining throughout the loading history, which may indicate potential bending of the pathfinder article as discussed previously. While $\varepsilon_{11}^{[SG3]} \approx \varepsilon_{11}^{[SG11]}$, on the other hand, $\varepsilon_{11}^{[SG4]} < \varepsilon_{11}^{[SG12]}$ throughout the loading history, as may be observed from Figure 8 (b) and Figure 8 (d). Whether this phenomenon is indicative of damage onset in the bottom side of the pathfinder article in the test configuration of Figure 7, is a matter of conjecture because the available visual evidence is not substantive.

The kink in the load-strain data corresponding to $\varepsilon_{11}^{Exp} \approx 9,000 \ \mu\varepsilon$ in Figure 8 (b) and Figure 8 (d), may indicate damage onset in the vicinity of the bag side interface between regions R_1 and R_2 and $R_{1'}$ and $R_{2'}$, respectively, as shown in Figure 6. The regions R_1 and R_2 and $R_{1'}$ and $R_{2'}$, are located near the top and bottom sides of pathfinder article, respectively, in the test configuration of Figure 7. The corresponding loads measured at damage onset are $P_{Exp}^{Ons}|_{Top} \approx 21,500 \ lbf$ (94,742 N) and $P_{Exp}^{Ons}|_{Bottom} \approx 18,200 \ lbf$ (27,078 N).
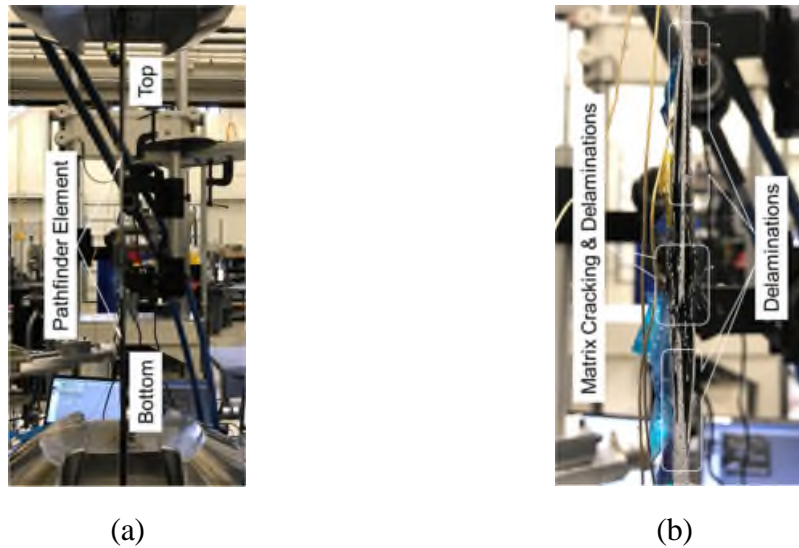

(a) (b)

Figure 7. (a) Pathfinder test article installed in the MTS testing machine. (b) Representative photograph showing the post-test side view of the damaged pathfinder article.

Based on the above data, it may now be reasonably surmised that damage onset occurs near the bottom of the pathfinder article in the test configuration of Figure 7. The mode damage onset cannot be deduced as the available evidence is not substantial. Furthermore, the absence of any kinks in the load-strain data in Figure 8 (c) and the linear nature of the same through the loading history, indicate that damage onset does not occur in the central thinner region of the pathfinder article, Figure 6. The combination of the above observations may be taken to indicate that the design intent of capturing damage initiation in the vicinity of the ply-drop regions has been achieved. Additional evidence in support of this deduction will be presented in the next section.

PRELIMINARY MODEL-TEST CORRELATIONS

Qualitative Comparisons of the Delamination Damage Mode

A qualitative comparison of the delamination damage mode predicted by the 2D models developed herein and captured experimentally is reported in Figure 9. The locations of the individual ply blocks and resin pockets are listed in Figure 4. The

modeling predictions in Figure 9 are reported as contour maps of the $CSDMG$ variable available as a field output in ABAQUS [22]. The above contours were generated when $CSDMG = 1.0$ for most of the length of the respective interfaces. Specifically, the red contours in Figure 9 representative of $CSDMG = 1.0$ are indicative of the complete failure/separation of the interface region, thereby simulating delaminations captured experimentally.
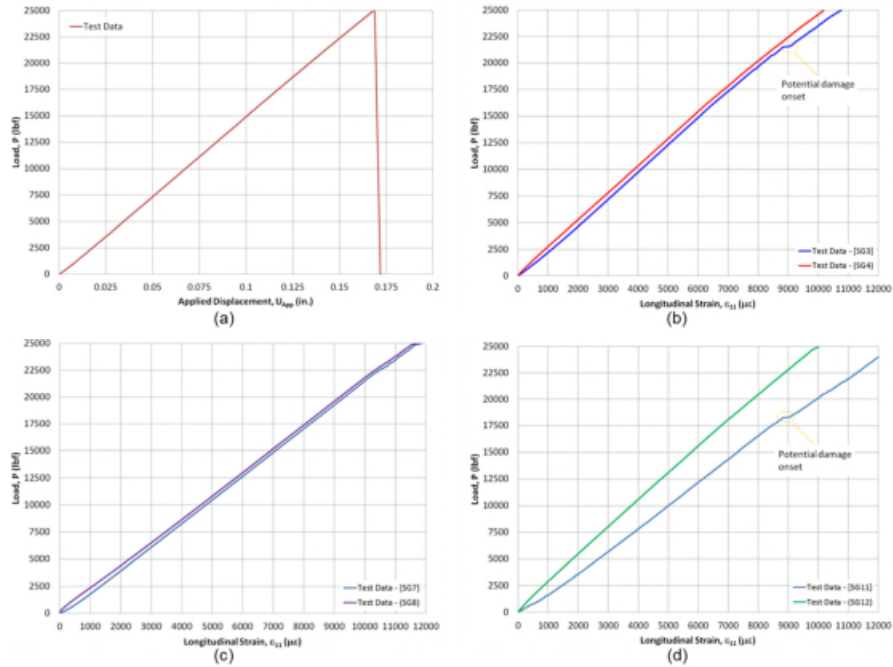

Figure 8. Experimentally captured quantitative data. (a) $P - U_{App}$ response. (b) $P - \varepsilon_{11}$ data for [SG3] and (SG4). (c) $P - \varepsilon_{11}$ data for [SG7] and (SG8). (d) $P - \varepsilon_{11}$ data for [SG11] and (SG12).

Upon reviewing Figure 9 (a) it may be surmised that the predictions for 'Delamination between Block2 and Resin Pocket' (i.e. Interface 1 in Figure 4), 'Delamination between Block1/Block2 and Resin Pocket' (i.e. Interface 2 in Figure 4) and 'Delamination between Block6 and Resin Pockets' (i.e. Interface 3 in Figure 4) qualitatively correlate with experimental evidence. Furthermore, the C-Scan images in Figure 9 (b) show the appearance of the delamination pattern as function of increasing load at the interface between the R1' and R2' regions, Figure 5. As shown at the bottom of Figure 9 (b), this delamination is predicted to grow along the interface between Block # 1 and Block # 2 (see Figure 4) toward the end regions of the pathfinder. These comparisons are consistent with experimental observations reported in Figure 9, thereby providing favorable preliminary qualitative correlations.

Comparisons of the Load-Displacement Response

The slope of the linear region of the load-displacement response, Figure 10, can be calculated as: K_{Exp} 148,810 $lbf/in.$ (26,059 N/mm). On the other hand, the slope of the predicted load-displacement response may be similarly computed as: $K_{Mod} =$

168,919 $lbf/in.$ (29,581 N/mm). The associated error is computed as: $K^{error} = \frac{K_{Mod}-K_{Exp}}{K_{Exp}} \times 100 = 13.68\%$, which implies that the model response is slightly stiffer than the experimental characterization. This is only to be expected since the model does not account for any manufacturing related inconsistencies such as variations in cross-sectional thickness, geometric imperfections near the vicinities of the ply-drops and any potential defects. Nevertheless, the prediction of the stiffness of the pathfinder article within $\pm 15\%$ of the experimental average is considered acceptable.

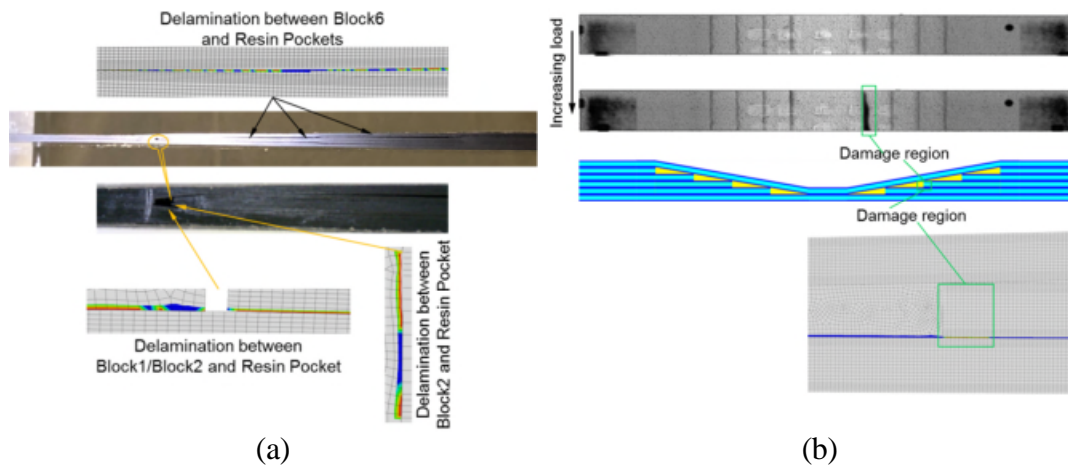(a)   (b)

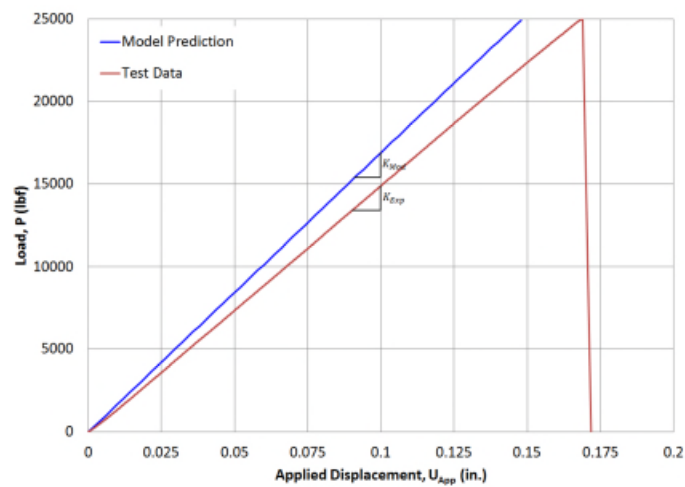Figure 9. Comparison of the predicted and observed locations of delaminations.

Figure 10. Comparison the predicted and measured load-displacement response.

Comparisons of the Load-Strain Response

In Figure 11, the predicted and measured $P - \varepsilon_{11}$ data for the strain gages [SG1], [SG3], [SG9] and [SG11] are reported. The data in Figure 11 reflects a mostly linear response until $\varepsilon_{11}^{Exp}|_{BagSide} \approx 9,000\ \mu\varepsilon$, at which point, the readings indicate an observable kink. As discussed previously, these kinks may correspond to damage onset. Since the kink recorded by [SG11] appears at the lowest load, it only be conjectured that damage onset may be occurring in the vicinity of the corresponding resin pocket/ply block interface. While the kinks are recorded more or less at the same strain level by all the gages, the associated loads vary by about 18% with respect to the lowest recorded load level: $P_{Ons}^{[SG11]} = 18,200\ lbf$ (80,954 N). This observation implies that on the taper side, the pathfinder article is subject to differential straining along the longitudinal (i.e. length) and transverse (i.e. width) directions perhaps due to manufacturing related inconsistencies, leading to the recorded scatter in the $P - \varepsilon_{11}$ data, Figure 11.

Since the models developed herein do not account for the aforementioned inconsistencies, the predictions reported in Figure 11 vary significantly from the experimental data. It should be noted that a kink in the predicted $P - \varepsilon_{11}$ response is reported in Figure 11, although the kink corresponds to $\varepsilon_{11}^{Mod}|_{BagSide} \approx 8,000\ \mu\varepsilon$ at which $P_{Ons}^{Mod} = 23,300\ lbf$ (103,638 N). The error in predicting the strain at damage onset on the taper side is calculated as: $\varepsilon_{11}^{error}|_{BagSide} = \frac{\varepsilon_{11}^{Mod}|_{BagSide} - \varepsilon_{11}^{Exp}|_{BagSide}}{\varepsilon_{11}^{Exp}|_{BagSide}} \times 100 = -11.11\%$. Similarly, the error in predicting the load at damage onset is computed as: $P_{Ons}^{error} = \frac{P_{Ons}^{Mod} - P_{Ons}^{Exp}}{P_{Ons}^{Exp}} \times 100 = 28\%$. The longitudinal strain at peak load is not correlated since the models do not capture the peak load.

Furthermore, at $\varepsilon_{11}^{Mod}|_{Ini} \approx 8,000\ \mu\varepsilon$, the longitudinal tensile stress in the off-axis $\pm 60°$ plies was determined from the 2D plane strain FE models as: $S_{11}^{\pm 60°}|_{Ons} \approx 27.5\ ksi$ (189.60 MPa). Comparing $S_{11}^{\pm 60°}|_{Ons} \approx 27.5\ ksi$ (189.60 MPa) with the predicted longitudinal strength $X_T^{\pm 60°} = 16.6\ ksi$ (164.25 MPa) listed in Table 1, it may be reasonably surmised that the kinks in Figure 11 may correspond to the failure of the off-axis 60°-plies.

DISCUSSIONS

The objective of this study was to computationally predict and experimentally capture delamination damage initiation in the vicinity of ply-drops. For the purpose of this study a tapered laminated composite structure (i.e. the pathfinder article) was designed, analyzed, fabricated and tested under displacement-controlled static tension loads. The CLT and CZM based design and analysis of the pathfinder article provided preliminary qualitative correlations with experimental data regarding the locations of delamination damage growth.

Comparisons of observed delaminations between resin rich regions and associated ply-drops, Figure 9, provide preliminary qualitative correlations between models and experiments. Matrix cracking in the off-axis plies, Figure 7, provides experimental

evidence of these damage modes. Overall, the predicted and expected damage modes were captured experimentally. However, the experimental methodology could not resolve whether the inter-laminar or the intra-laminar damage mode was triggered first. Future studies will aim to refine the experimental methodology by including incremental X-Ray Computed Tomography (X-Ray CT) imaging to capture the mode of damage initiation and subsequent growth.

CONCLUSIONS

A relatively simple methodology for predicting the damage initiation mode in tapered laminated composite structures under static tension loads was developed in this study. As part of this effort, it was shown that the design of the tapered laminated composite structure could be developed in a manner that fosters inter-laminar delamination initiation and growth over intra-laminar damage modes. While the mode of damage initiation could not be captured experimentally, delaminations in general, were shown to be the major damage drivers in the tapered laminated composite structure. Furthermore, the initial structural stiffness of the tapered laminated composite structure and the longitudinal strain corresponding to damage onset were predicted within 15% of the corresponding experimental data. Additionally, preliminary qualitative correlations of predicted and experimentally observed delamination damage modes were presented.
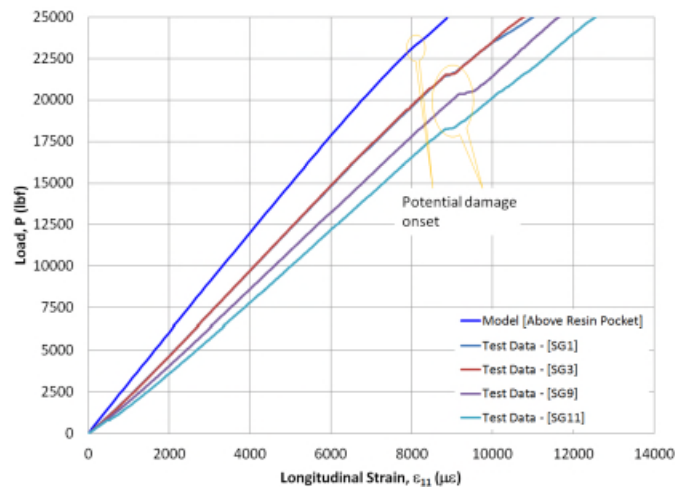
ACKNOWLEDGEMENTS

Figure 11. Comparison of predicted and measured $P - \varepsilon_{11}$ response.

REFERENCES

1. Leone, F. A. 2015. "Deformation Gradient Tensor Decomposition for Representing Matrix Cracks in Fiber-Reinforced Composite Structures," Composites Part A: Applied Science and Manufacturing, 76: 334–341.
2. Nikishkov, Y., A. Makeev, and G. Seon. 2013. "Progressive fatigue damage simulation method for composites," International Journal of Fatigue, 48:266–279.
3. Chen, B.Y., S.T. Pinho, N.V. De Carvalho, P.M. Baiz, and T.E. Tay. 2014. "A Floating Node Method for the Modelling of Discontinuities in Composites," Engineering Fracture Mechanics, 127:104–134.
4. Krueger, R. 2004. "Virtual Crack Closure Technique: History, Approach, and Applications," Applied Mechanics Reviews, 57(2):109–143.
5. Turon, A., P.P. Camanho, J. Costa, and J. Renart. 2010. "Accurate Simulation of Delamination Growth under Mixed-Mode Loading using Cohesive Elements: Definition of Interlaminar Strengths and Elastic Stiffness," Journal of Composite Structures, 92(8):1857–1864.
6. Iarve, E.V., M.R. Gurvich, D.H. Mollenhauer, C.A. Rose and C.G. Dávila. 2011. "Mesh-independent matrix cracking and delamination modeling in laminated composites," International Journal of Numerical Methods in Engineering, 88(8):749 – 773.
7. *Anonymous*. 2006. "Guide for Verification and Validation in Computational Solid Mechanics," The American Society of Mechanical Engineers ASME V&V 10-2006.
8. *Anonymous*. 2012. "An Illustration of the Concepts of Verification and Validation in Computational Solid Mechanics," The American Society of Mechanical Engineers ASME V&V 10.1-2012.
9. Krueger, R. 2010. "Development of a Benchmark Example for Delamination Fatigue Growth Prediction," NASA CR-2010-216723.
10. Krueger, R. 2011. "Development and Application of Benchmark Examples for Mode II Static Delamination Propagation and Fatigue Growth Predictions," NASA CR-2011-217305.
11. Krueger, R. 2012. "Development and Application of Benchmark Examples for Mixed-Mode I/II Quasi-Static Delamination Propagation Predictions," NASA CR-2012-217562.
12. De Carvalho, N.V., and R. Krueger. 2016. "Modeling Fatigue Damage Progression and Onset in Composites using an Element-Based Virtual Crack Closure Technique Combined with the Floating Node Method," in *Proceedings of the American Society for Composites 31st Technical Conference*, Williamsburg, VA, USA.
13. Wanthal, S., J. Schaefer, B. Justusson, I. Hyder, S. Engelstad and C. Rose. 2017. "Verification and Validation Process for Progressive Damage and Failure Analysis Methods in the NASA Advanced Composites Consortium," in *Proceedings of the American Society for Composites 32nd Technical Conference*, West Lafayette, IN.
14. Cui, X., X. Ren, P. Liu, J. Lua, P.M. Rao, M.D. Mordasky, and M.R. Gurvich. 2018. "A Dual Spring Modeling Approach for Static and Fatigue Failure Assessments of Carbon/Epoxy Composite Sub-Elements," *AIAA/ASCE/AHS/ASC Structures, Structural Dynamics, and Materials Conference*, 8–12 January 2018, Kissimmee, Florida.
15. Rao, P.M., M.D. Mordasky, M.R. Gurvich, N. de Carvalho, B.R. Seshadri, and J.G. Ratcliffe. 2018. "Validation of a Discrete Damage Mechanics Methodology Using the Static and Fatigue Behavior of Carbon/Epoxy Tapered Specimens," *AIAA/ASCE/AHS/ASC Structures, Structural Dynamics, and Materials Conference*, 8–12 January 2018, Kissimmee, Florida.
16. Seshadri, B.R., N.V. de Carvalho, L.R. Deobald, G.E. Mabson, and J.G. Ratcliffe. 2018. "Simulating the Clamped Tapered Beam Specimen under Quasi-Static and Fatigue Loading," *AIAA/ASCE/AHS/ASC Structures, Structural Dynamics, and Materials Conference*, 8–12 January, Kissimmee, Florida.

17. M.R. Wisnom, R. Dixon and G. Hill. 1996. "Delamination in Asymmetrically Tapered Composites Loaded in Tension," *Composite Structures*, 35:309–322.

18. Makeev, A., Y. Nikishkov, G. Seon, and E. Lee. 2016. "Analysis Methods Improving Confidence in Material Qualification for Laminated Composites," in *Proceedings of the American Helicopter Society 72nd Annual Forum*, West Palm Beach, FL.

19. Murri, G.B. 2013. "Evaluation of Delamination Onset and Growth Characterization Methods under Mode I Fatigue Loading," NASA/TM-2013-21766..

20. O'Brien, T. K., W.M. Johnston, and G.J. Toland. 2010. "Mode II Interlaminar Fracture Toughness and Fatigue Characterization of a Graphite Epoxy Composite Material," NASA/TM-2010-216838.

21. Benzeggagh, M. and M. Kenane. 1996. "Measurement of Mixed-Mode Delamination Fracture Toughness of Unidirectional Glass/Epoxy Composites with Mixed-Mode Bending Apparatus," *Composite Science and Technology*, 56:439–449, 1996.

22. ABAQUS/Standard User's Manual. Dassault Systemes Simulia, Pawtucket, Rhode Island, USA.

23. Leone, F. A., C. G. Davila, G. E. Mabson, M. Ramnath and I. Hyder. 2017. "Fracture-Based Mesh Size Requirements for Matrix Cracks in Continuum Damage Mechanics Models," in *AIAA/ASCE/AHS/ASC Structures, Structural Dynamics, and Materials Conference*, Grapevine, TX.

24. Jones, R.M. 1999. "Mechanics of Composite Materials," 2nd Edition, Taylor and Francis.

25. Karkkainen, R.L., Sankar, B.V. 20016. "A direct micromechanics method for analysis of failure initiation of plain weave textile composites," *Composites Science and Technology*, 66:137 – 150.

26. Rao, M.P., B.V. Sankar, and G. Subhash, 2009. "Effect of Z-yarns on the stiffness and strength of three-dimensional woven composites," *Composites: Part B*, 40: 540 – 551.

27. *Anonymous*. 2011. Test Report Number: CAM-RP-2009-015 Rev A, National Center for Advanced Materials Performance, National Institute for Aviation Research, Wichita State University.

28. *Anonymous*. Document Number: NPS 81228, Revision B, National Center for Advanced Materials Performance, National Institute for Aviation Research, Wichita State University.